Structure

A drug and ATP binding site in type 1 ryanodine receptor

Graphical abstract

Highlights

- High-resolution structure of RyR1 reveals second binding site for ATP

- ATP and ARM210 bound simultaneously in binding site located in cytosolic shell

- Binding of ARM210 is dependent on ATP and stabilizes closed state of the channel

- Unique binding modes between ATP and ADP suggest role as metabolic sensor
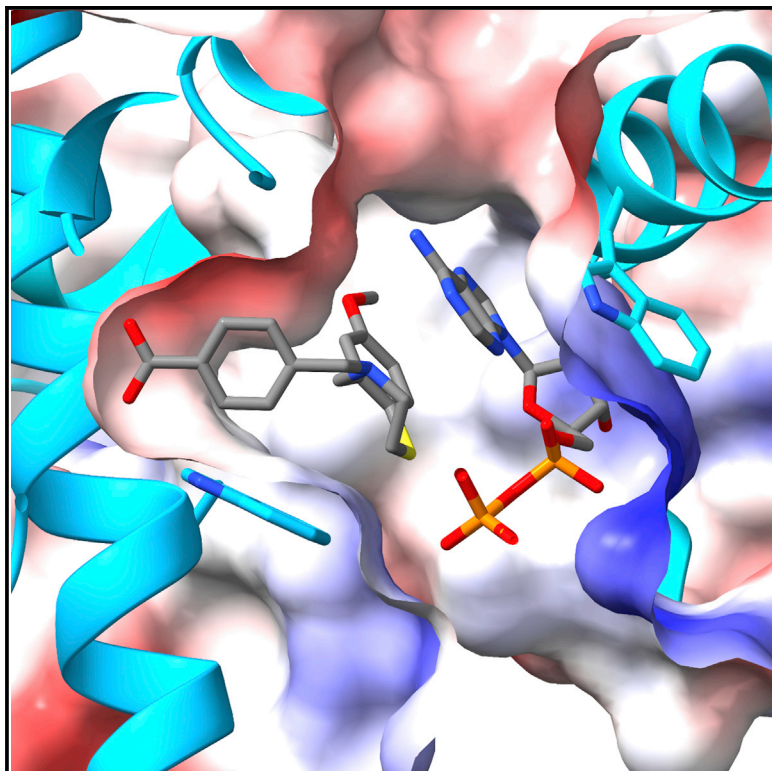
Authors

Zephan Melville, Haikel Dridi, Qi Yuan, ..., Yang Liu, Oliver B. Clarke, Andrew R. Marks

Correspondence

arm42@cumc.columbia.edu

In brief

Melville et al. show the cryo-EM structure of the ARM210-bound ryanodine receptor. The Rycal compound (ARM210) binds cooperatively with ATP in a second ATP-binding site and stabilizes the closed state of the channel. This site may be a metabolic sensor as it binds two ADP but only one ATP.

CellPress

Article

A drug and ATP binding site in type 1 ryanodine receptor

Zephan Melville,[1] Haikel Dridi,[1] Qi Yuan,[1] Steven Reiken,[1] Anetta Wronska,[1] Yang Liu,[1] Oliver B. Clarke,[1,2] and Andrew R. Marks[1,3,4,*]

[1]Department of Physiology and Cellular Biophysics, Columbia University, New York, NY, USA
[2]Department of Anesthesiology, Columbia University, New York, NY, USA
[3]Clyde & Helen Wu Center for Molecular Cardiology, Columbia University, New York, NY, USA
[4]Lead contact
*Correspondence: arm42@cumc.columbia.edu
https://doi.org/10.1016/j.str.2022.04.010

SUMMARY

The ryanodine receptor (RyR)/calcium release channel on the sarcoplasmic reticulum (SR) is required for excitation-contraction coupling in skeletal and cardiac muscle. Inherited mutations and stress-induced post-translational modifications result in an SR Ca^{2+} leak that causes skeletal myopathies, heart failure, and exercise-induced sudden death. A class of therapeutics known as Rycals prevent the RyR-mediated leak, are effective in preventing disease progression and restoring function in animal models, and are in clinical trials for patients with muscle and heart disorders. Using cryogenic-electron microscopy, we present a model of RyR1 with a 2.45-Å resolution before local refinement, revealing a binding site in the RY1&2 domain (3.10 Å local resolution), where the Rycal ARM210 binds cooperatively with ATP and stabilizes the closed state of RyR1.

INTRODUCTION

Located on the sarco-/endoplasmic reticulum (SR/ER) membrane, the ryanodine receptor (RyR) is the largest known ion channel, at over 2 MDa, and is the primary mediator of the Ca^{2+} release required for excitation-contraction coupling in cardiac and skeletal muscle. RyR1 is the primary isoform in skeletal muscle, while RyR2 is the predominant cardiac isoform. RyR1 and RyR2 are also found in neurons. Beyond their expression pattern, RyR1 and RyR2 are unique in how each is activated. In skeletal muscle, RyR1 is activated by mechanical coupling with the dihydropyridine receptor (Nakai et al., 1996). RyR2 is instead activated by Ca^{2+} in the process called Ca^{2+}-induced Ca^{2+} release (Fabiato and Fabiato, 1978), in which Ca^{2+} binding to RyR2 creates a cascade effect, and the release of Ca^{2+} through RyR2 creates a high local concentration of Ca^{2+}, which can cause neighboring RyR2 channels to open. RyR1, itself a homotetramer comprising four RyR1 monomers, forms arrays in skeletal muscle on the terminal cisternae of the SR, and under normal conditions, undergoes cooperative activation through a process called coupled gating (Marx et al., 1998, 2001; Porta et al., 2012; Zalk and Marks, 2017).

The correct activation of RyRs, and thus activation of the appropriate downstream Ca^{2+} signaling pathways, is regulated by numerous ligands and protein interactions, including, most recently, diamides (Ma et al., 2020). Aside from Ca^{2+}, ATP, and caffeine, RyR1 also binds calmodulin (CaM), which acts as an activator under low $[Ca^{2+}]_{cyt}$ (<1 μM) and as an inhibitor of RyR1 under high $[Ca^{2+}]_{cyt}$ (>1 mM), which occurs locally

following intracellular Ca^{2+} release. Calstabin-1 is a subunit of RyR1 that stabilizes the closed state of the channel (Brillantes et al., 1994); however, in disease states, RyR can be oxidized and phosphorylated, which causes calstabin to dissociate from the channel (Marx et al., 2000; Shan et al., 2010). This results in SR Ca^{2+} leaking into the cytosol and inappropriate triggering of downstream Ca^{2+} signaling pathways (Andersson et al., 2011; Marx et al., 2000; Wehrens et al., 2003, 2006). As a key player in Ca^{2+} signaling, leaky RyR channels are associated with a wide variety of disease states, including muscular dystrophy (Bellinger et al., 2009) and myopathies (Kushnir et al., 2020), heart failure (Lehnart et al., 2004, 2006; Marx et al., 2000; Reiken et al., 2003; Wehrens et al., 2003), diabetes (Santulli et al., 2015), and neurological disorders including post-traumatic stress disorder (PTSD) (Liu et al., 2012), Huntington's disease (Dridi et al., 2020), and Alzheimer's disease (Lacampagne et al., 2017). Given the critical role of the RyR in Ca^{2+} signaling, our lab has worked to create and validate a class of therapeutics designed to prevent the RyR-mediated intracellular Ca^{2+} leak that occurs in disease states. This work has led to the creation of Rycals, a class of orally available benzothiazepine derivatives that bind directly to the RyR and prevent the Ca^{2+} leak (Andersson and Marks, 2010; Bellinger et al., 2008; Wehrens et al., 2004).

Our work has shown the efficacy of these compounds both *in vitro* and *in vivo* in animal models of human diseases (Andersson and Marks, 2010; Bellinger et al., 2008; Wehrens et al., 2004) and *ex vivo* in samples from human patients (Capogrosso et al., 2018; Fauconnier et al., 2010; Kushnir et al., 2018; Lacampagne et al., 2017; Shan et al., 2012). The Rycals prevent SR Ca^{2+} leak by

binding to the RyR and causing the reassociation of calstabin, thus stabilizing the closed state of the channel. Mutations in RyR have been linked to rare genetic forms of cardiac and skeletal muscle disorders; Rycals have proven effective in these forms in animal models (Bellinger et al., 2009; Kushnir et al., 2020; Lacampagne et al., 2017; Lehnart et al., 2008; Santulli et al., 2015; Waning et al., 2015; Wehrens et al., 2004, 2005). One such compound, called ARM210, is a second-generation Rycal that is currently in clinical trials for patients with RyR1 myopathy, an inherited disorder characterized by progressive muscle weakness (https://clinicaltrials.gov/ct2/show/NCT04141670). Given the structure of the Rycal compounds, which are primarily aromatics and charged groups, they were initially hypothesized to bind near the caffeine-binding site based on early cryoelectron microscopy (cryo-EM) structures with limited resolution. Since then, advances in cryo-EM have dramatically improved the resolution of cryo-EM maps, making it possible to unambiguously identify ligand-binding sites, including ATP, Ca^{2+}, and caffeine (des Georges et al., 2016; Melville et al., 2021). These advances include direct detection cameras, optimization of the defocus range during data collection, and processing methods such as symmetry expansion and local refinement.

Ultimately, these improvements have shown that there is a second ATP-binding site, in the periphery of the cytosolic shell of the RyR, in the RY1&2 domain, a region previously too dynamic and disordered to make clear conclusions concerning ligand binding. Given the structural similarity between the adenosine of ATP and the benzothiazepine moiety of ARM210, we hypothesized that this could be the Rycal-binding site as well. We now show that the Rycal compound ARM210 binds in the RY1&2 domain cooperatively with ATP and stabilizes the closed state despite the presence of activating ligands (Ca^{2+}, ATP, and caffeine). These results were confirmed functionally using site-directed mutagenesis and electrophysiology. This identifies ARM210 as an allosteric regulator, and we expect that this binding site could also serve as a metabolic sensor as it binds one molecule of ATP or two molecules of ADP, and ATP is a more potent activator of RyR channels (Kermode et al., 1998). As this is a structure of the channel in complex with a therapeutic compound, these data will enable the optimization of the Rycal compounds as well as provide insight into their mechanism of action.

RESULTS

Structure of the ligand-bound ryanodine receptor

RyRs are homotetrameric macromolecular complexes comprising three major regions, each composed of several domains and segments. The cytosolic shell consists of the N-terminal domain (NTD) with two segments (A & B) and an N-terminal solenoid, three SPRY domains, two RYR domains (RY1&2 and RY3&4), and the junctional and bridging solenoids (J-Sol and Br-Sol) (Zalk et al., 2015; Zalk and Marks, 2017). The cytosolic shell also contains the calstabin binding site, which consists of a hydrophobic pocket formed by the Br-Sol and SPRY1 domains. Calmodulin binds on the other side of the Br-Sol from calstabin, with the N-terminal domain of CaM binding along the face of the Br-Sol, while the C-terminal domain binds a peptide within a pocket of the Br-Sol.

Ca^{2+}, ATP, and caffeine bind within the C-terminal domain (CTD) of RyR1, and the RY1&2, within the SPRY domains, forms the second ATP-binding site (Figure 1, Videos S2 and S3). Here, ARM210 and ATP simultaneously occupy the binding site with ATP bound on the interior, pi-stacking with W996, while ARM210 is bound on the periphery, pi-stacking with W882 and the adenine ring of ATP. The ribose ring is also supported by N1035, while the triphosphate tail is further supported by salt bridges with H993, R1000, N1018, R1020, and potentially R886 and R897, although the density for this is limited. Several potential interactions exist for the benzoic acid tail of ARM210; however, the density for this moiety and the surrounding region is too ambiguous to make clear conclusions, save for a salt bridge with H879 and potentially N921. ARM210 is also positioned such that it may form a methionine-aromatic bridge with M924. The residues that are close enough to form hydrophobic or hydrogen bonding interactions are highlighted in Figure 1 and the potential salt bridges are shown in Figure S1. CryoEM statistics are summarized in Table 1.

Binding of ATP and ARM210

Rycal binding (B-max) to RyR1 is increased ~10-fold by oxidation and phosphorylation of the channel (Table 2), mimicking the condition of RyR in disease states (Figure 2A), and Rycal binding was increased by a similar degree in the presence of 10 mM ATP (Figure 2B; Table 2). The similarities between the adenine ring of ATP and the benzothiazepine moiety of Rycal compounds (Figure 1) provided sound reasoning to test this site for Rycal binding using a radiolabeled form of a first-generation Rycal, S107, which competes with ARM210 for the binding site in RyR1 (Figure 2C; Table 2). When equal concentrations of ARM210 and ^{3}H-S107 were present (500 nM each), ^{3}H-S107 binding also decreased 2-fold, indicating the increased affinity of ARM210 compared to S107 (Figure 2C). This follows in accordance with the structures of S107 and ARM210, as the former is a scaffold lacking the benzoic acid tail of the latter and both bear similarities to the adenine ring of ATP, while the benzoic acid tail of ARM210 resembles the ribose ring and tail (Figure 1).

After resolving the structure of RyR1 in the presence of ARM210, we confirmed the binding by mutating the primary binding residue (W882A) and found that this abolished ^{3}H-S107 binding to the channel (Figure 2E). In contrast, ATP binding was maintained, although slightly reduced with RyR1-W882A, as evidenced by the decreased affinity of radiolabeled ATP (Figure 2F); however, ATP binding was significantly reduced in the W996A mutant (Figure 2G). In this instance, ATP binding is partially retained at the C-terminal binding site in RyR1 (des Georges et al., 2016). Finally, ARM210 binding was also abolished in W996A, likely as a result of the loss of ATP binding in the RY1&2 binding pocket (Figure 2H).

These experiments were then repeated with ADP in place of ATP to compare ADP binding to this site (Figures 2I–2L). ADP exhibited similar binding to WT-RyR1, with the exception of greater stoichiometry, with 12 molecules of ADP per channel compared to a maximum of 8 with ATP, wherein the C-terminal site is occupied by one molecule of either ligand. Likewise, ADP binding remained greater than one molecule per channel in RyR1-W996A, indicating the binding of two molecules of ADP to the peripheral binding site, whereas only a single ATP binds to this site. To
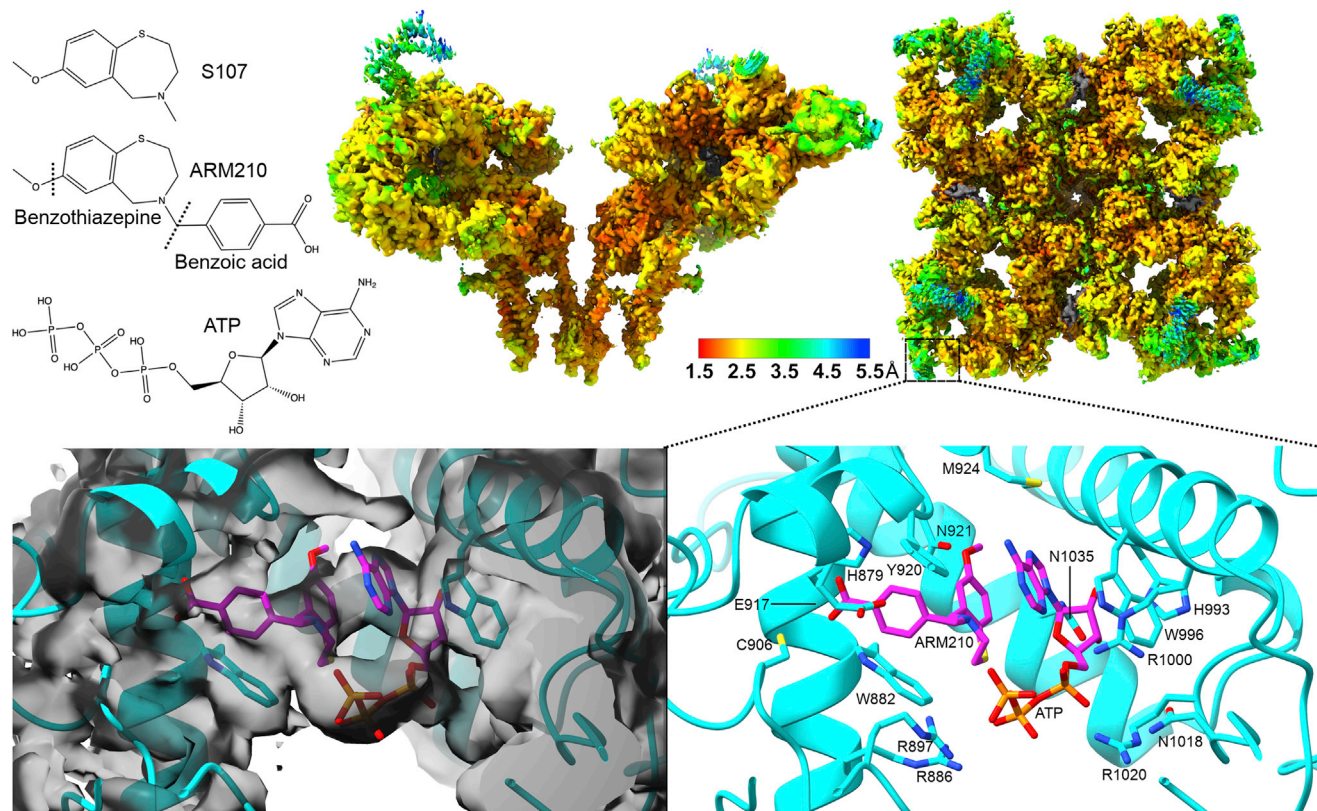
Figure 1. Binding site

(Top) Chemical structures of S107, ARM210, and ATP; side and top view of RyR1 colored by resolution after local refinement. Two opposing protomers are shown in the side view and a small strip (gray) is visible in the BrSol where local refinement maps did not overlap. (bottom) Top view of the ARM210 and ATP binding site within the RY1&2 domain with and without Coulombic density. ARM210 binds in the periphery, pi-stacking with W882, while ATP binds on the interior, forming the same interaction with W996 through the ribose ring and ARM210 through the adenine ring. Both ligands are further stabilized by a series of charge interactions with arginine and histidine. See Figure S1 for the potential salt bridge distances, Videos S1 and S2 for additional viewing angles of the local resolution and binding site, and Video S3 for a comparison of the flexibility and resulting resolution of the periphery and interior of the RY1&2 domain.

confirm this and to assess the competition between ADP and Rycal binding, S107 binding was measured in the presence of increasing concentrations of ATP or ADP (Figure 2D). In this experiment, no competition was observed in the presence of ATP; however, high concentrations of ADP were found to have a significant inhibitory effect on the binding of S107. Notably, this required significantly higher than physiological concentrations, as Rycals exhibit a much higher affinity. These data indicate that the additional occupancy of ADP is in the same Rycal-binding site and that the binding of ATP and ADP are not identical.

Physiology and function

To characterize the role of the periphery of the RY1&2 in the binding and stabilizing effects of ARM210, we mutated C906 to alanine in addition to W882. The open probability (P_o) of these channels correlated with that of wild-type (WT) channels under resting conditions (150 nm Ca^{2+}) and following treatment with H_2O_2 to trigger the oxidation-induced Ca^{2+} leak, indicating that these mutants remain functional; however, the Ca^{2+} leak was not rescued by the addition of ARM210 in W882A and showed only a minor reduction for C906A (Figures 3A and 3B). These re-

sults were further confirmed by Ca^{2+} imaging, wherein Ca^{2+} release was measured in response to the caffeine-induced activation of RyR1 (Figure 3C). In this experiment, oxidation of RyR1 causes a leak that depletes intracellular Ca^{2+}, blunting the response to caffeine-induced Ca^{2+} release. Both mutants were unaffected by ARM210 and only the WT channels could be restored to stable conditions following oxidation. These results corroborate the fact that the binding site of ARM210 resides in the RY1&2 domain and indicate that residues in the periphery of the RY1&2 are critical in the allosteric regulation by ARM210; in addition, the mutation of C906 does not confer protection against the oxidation-induced leak.

Conformation and conservation

ARM210 and ATP binding to the RyR causes a significant conformation change in the RY1&2 domain (Figure 4, Video S4). In the unbound state, the RY1&2 domain is open, as it has been viewed in previously published structures, whereas the ATP- and ARM210-bound state shows the periphery of the domain closing around the aforementioned ligands, with the exception of the top-most helix, which bends outward to accommodate ARM210. Sequence alignments indicate that the critical residues of the RY1&2 domain are

Table 1. cryo-EM Statistics

Data collection	
Microscope	FEI Titan Krios
Detector	Gatan K3
Voltage, kV	300
Magnification	105,000
Exposure, e$^-$/Å^2	57.65
Defocus range, μm	−1 to −2
Pixel size, Å	0.833
Processing	
Software	cryoSPARC
Symmetry	C4
Initial particles, N	333,010
Final particles, N	153,840
Map resolution, Å	2.45[a]
Map resolution range, Å	2.24–2.57[b]
Model composition	
Peptide chains	12
Nonhydrogen	149,472
Protein residues	18,644
Ligands	44
Mean B factors (Å^2)	
Protein	78.20
Ligands	89.69
RMSDs	
Bond length, Å	0.003
Bond angles, °	0.496
Ramachandran, %	
Favored	97.52
Allowed	2.48
Disallowed	0.00
Validation	
MolProbity score	1.58
Clashscore	5.12
Rotamer outliers, %	1.90
PDB ID	7TZC
EMDB ID	26205

EMDB, Electron Microscopy Data Bank; PDB, Protein Data Bank; RMSD, root-mean-square deviation.

[a]Map resolution is the result of refinement in cryoSPARC before symmetry expansion and local refinement.

[b]Map resolution range represents the range of the averages determined by local refinement in cryoSPARC using the local masks described in STAR Methods.

Table 2. Radioligand binding

^{3}H-S107 with ATP	Kd (nM)	Bmax (mol S107/RyR1)
Untreated	150 ± 7	0.4 ± 0.1
PKA/H$_2$O$_2$	155 ± 9	3.7 ± 0.2
No ATP	147 ± 6	0.4 ± 0.1
10 mM ATP	152 ± 7	3.0 ± 0.2
RyR1-WT	200 ± 11	3.5 ± 0.3
RyR1-W882A	no binding	–
RyR1-W996A	no binding	–
^{32}P-ATP	Kd (mM)	Bmax
RyR1-WT	1.0 ± 0.1	8.0 ± 0.6
RyR1-W882A	5.0 ± 0.4	7.5 ± 0.6
RyR1-W996A	4.5 ± 0.3	2.5 ± 0.4
^{3}H-S107 with ADP	Kd (nM)	Bmax
RyR1-WT	188 ± 12	3.6 ± 0.3
RyR1-W882A	no binding	–
RyR1-W996A	250 ± 10	2.0 ± 0.2
^{32}P-ADP	Kd (mM)	Bmax
RyR1-WT	1.0 ± 0.1	12.0 ± 1.1
RyR1-W882A	3.0 ± 0.3	11.6 ± 0.6
RyR1-W996A	2.5 ± 0.3	6.0 ± 0.6

the pore (Figure 5) in the presence of ARM210 (indicated by the lack of a red or blue tint in the center), and the reaction coordinate scatterplot of the eigenvectors show that only one state (closed) is present. No significant conformation changes were found in other domains as a result of Rycal binding, although the closing of the RY1&2 domain was accompanied by improved resolution, making it possible to resolve ligand binding.

The improved resolution also allowed for additional assignments in numerous unstructured loops in addition to corrections made in the bridging and central solenoids, namely the addition of a short helix (3,472–3,479) and the correcting of a mismodeled helix (4224–4254), which was evident by the side-chain density of three phenylalanine residues (4,234, 4,237, and 4,243) (Figure S1). Representatitive side-chain densities for two protomers and for the SPRY domains and calstabin, as well as BrSol and CaM, are shown in Figure S3 along with Videos S5, S6, and S7.

While there are changes in the conformation of CaM compared to published structures (Woll et al., 2021), we expect that the differences are the result of Ca^{2+} binding to CaM along with significantly improved resolution, particularly regarding the c-lobe (Figure S4). While the binding site of calstabin is unchanged, this is to be expected for a WT channel. To resolve conformation changes as a direct result of Rycal binding, a mutant channel lacking calstabin will be required. Finally, The RY3&4 domain also contains the necessary residues to allow ATP binding with W2776 and W2886 along with various His and Lys residues; however, the binding of ATP and ADP were not indicated by the stoichiometry in radioligand binding experiments. Likewise, this domain adopts a much wider conformation that may leave the supporting His and Lys residues too far away to coordinate ligands, although, unfortunately, this domain shows the most limited resolution and is far too dynamic to be resolved by cryo-EM (Figure 1).
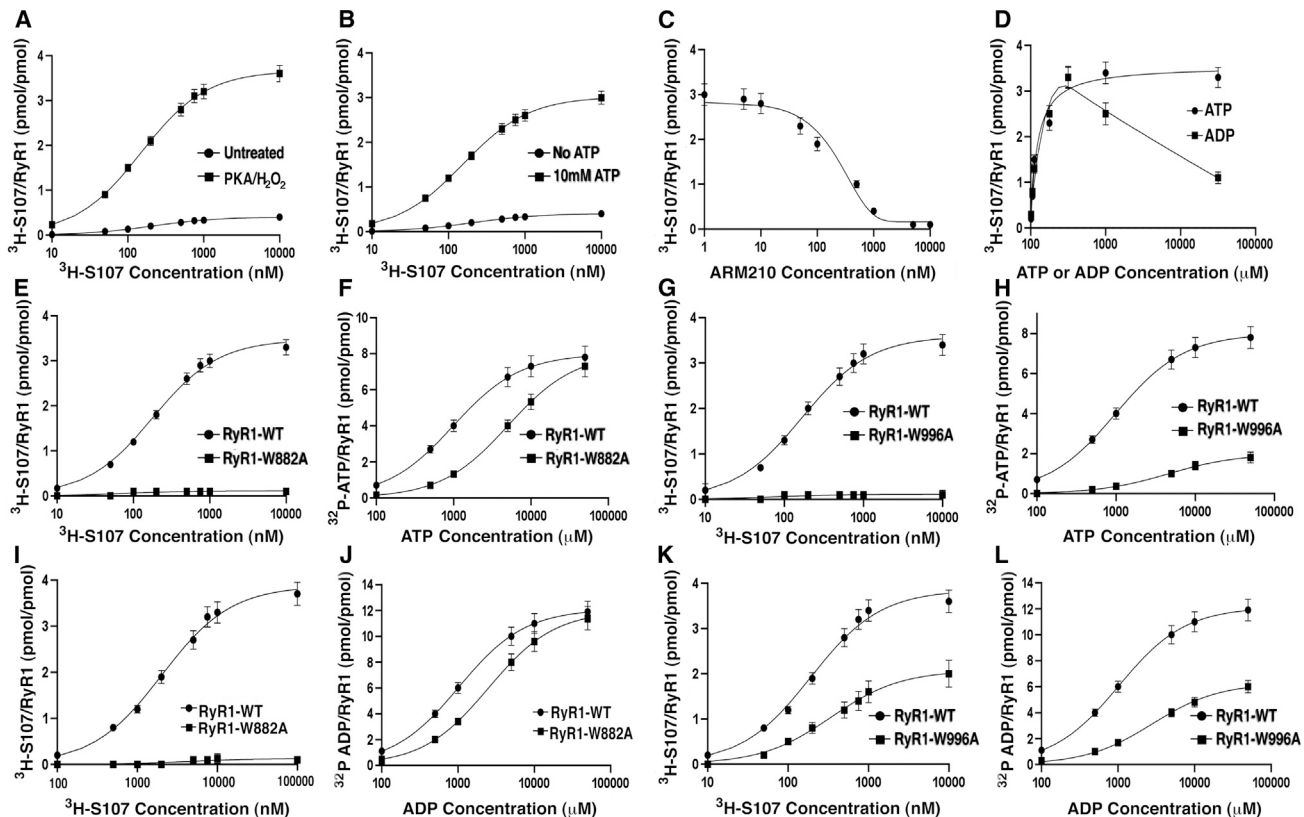
also conserved between RyR1, 2, and 3, as well as across different sources, including W882, W996, C906, and the many arginine residues that support the phosphate tail of ATP.

The pore of the channel was also found to be closed despite the presence of Ca^{2+}, ATP, and caffeine (Figure 4). These ligands were sufficient to push the channel into a primed state, with a significant (30%–60%) proportion of the channels being in the open state; however, no channels were found to be in the open state in the presence of ARM210. 3D variability slices show no variation in

Figure 2. Rycal binding

^{3}H-S107 binding performed in native rabbit microsomes (A–C) used only the endogenous ATP, while assays with recombinant RyR1 in HEK293 microsomes include the addition of 10 mM ATP (E–G) or ADP (I–K).

(A) Effects of PKA phosphorylation and oxidation of RyR1 on S107 binding. Binding was performed with untreated microsomes and microsomes treated with PKA and 1.0 mM H_2O_2.

(B) Effects of ATP on S107 binding to purified RyR1.

(C) S107-ARM210 competition performed with PKA/H_2O_2 treated microsomes, 500 nM of ^{3}H-S107, and varied concentrations (1–10,000 nM) of unlabeled ARM210.

(D) S107 binding in the presence of increasing concentrations of ATP or ADP.

(E) S107 binding to recombinant RyR1-WT and RyR1-W882A mutant in microsomes treated with PKA and H_2O_2.

(F) ^{32}P-ATP binding to WT and W882A RyR1.

(G) S107 binding to recombinant RyR1-WT and RyR1-W996A.

(H) ^{32}P-ATP binding to WT and W996A RyR1.

(I–L) Radioligand binding to WT and mutant channels with ADP in place of ATP. Expression of RyR1-W882A and W996A channels were confirmed by ^{3}H-ryanodine binding comparable to RyR-WT microsomes. Error bars represent the SD of the mean from 4 replicates.

DISCUSSION

Rycal compounds are benzothiazepine derivatives. Some benzothiazepine compounds are voltage-gated Ca^{2+} channel blockers (Capogrosso et al., 2018; Reiken et al., 2003; Wehrens et al., 2005), but, of critical importance, Rycal compounds do not exhibit any channel-blocking activity (Figure 3) (Andersson et al., 2011; Kushnir et al., 2020; Mei et al., 2013). This is likely tied to the mechanism of stabilizing the closed state of the RyR without outright inhibiting the channel. It may explain the persistent dynamics in the periphery of the RY1&2 domain (Figure 1; Videos S2 and S3), as we expect the closing of this domain is not dependent on the binding of ARM210 and can occur with ATP and ADP. It is instead the stabilization of this domain and the resulting closed state of the channel that is unique to Rycal binding, as the channels open normally in the presence of the endogenous ligands.

The usefulness of such a compound as a therapeutic is potentially significant as RyR leaks Ca^{2+} in disease states because the closed state of the channel becomes destabilized either due to oxidation and phosphorylation or due to inherited mutations that cause the stabilizing subunit, calstabin, to dissociate from the channel (Lehnart et al., 2008; Marx et al., 2000; Wehrens et al., 2003; Yano et al., 2000; Zalk and Marks, 2017). Our lab and others (Acimovic et al., 2018; Capogrosso et al., 2018; Fauconnier et al., 2010; Lacampagne et al., 2017; Mei et al., 2013) have shown that in disease models involving leaky RyR in cells, animals, and patients, treatment with a Rycal compound reverses the leak and restores calstabin binding. The mechanism for such a dramatic reversal remains unknown, but the structure
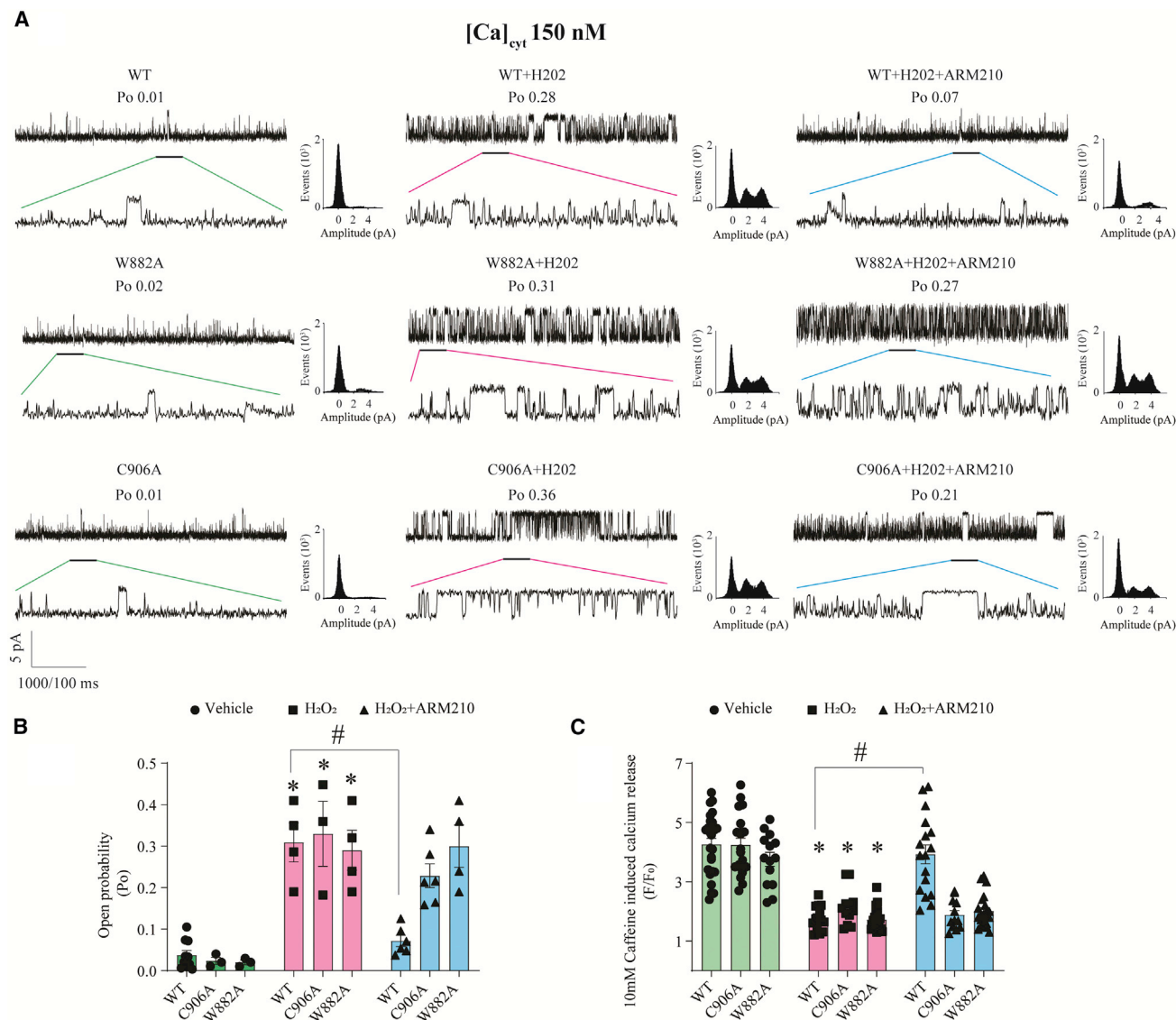
Figure 3. Single-channel recordings of wild-type (WT) and mutant RyR1 reconstituted in planar lipid bilayer

(A) Sections of each trace are shown with expanded timescale to demonstrate subconductance states. Opening events are recorded as an upward deflection. P_o = opening probability.

(B and C) Quantification of single channel (B) and (C) caffeine-induced calcium release in response to 10 mM caffeine in HEK293 cells expressing WT or mutant RyR1 channels. F is the maximal Ca^{2+} fluorescence signal and F0 is the fluorescence at resting Ca^{2+}. Microsomes and transfected cells were incubated with 1 mM H_2O_2 for 30 min at 37°C to induce oxidation. Treated samples were incubated with ARM210 (10 μM) overnight. Experiments were repeated at least 3 times. n ≥ 30 cells per group. Data are means ± SEMs; 1-way-ANOVA shows *p < 0.05 versus WT.

described here represents a significant step toward elucidation, in particular, the finding that ARM210 is sufficient to stabilize the closed state in the presence of Ca^{2+}, ATP, and caffeine (Figure 5). This mechanism may also be important in RyR arrays as the RY1&2 domain occupies a vital point of interaction between the channels on native SR membranes (Cabra et al., 2016; Inui et al., 1987; Samsó, 2017).

Previously, studies of Rycal binding were performed primarily in microsomes and early attempts to study Rycal binding to purified RyR have largely been unsuccessful. The primary targets for overcoming this hurdle had been the reconstitution of the channel complex by the addition of accessory proteins such as

CaM or the reconstitution of the lipid membrane itself using nanodiscs or liposomes. While the addition of CaM significantly improved the overall resolution, it was ultimately the addition of ATP to match cellular levels (5–10 mM) that reconstituted ARM210 binding to purified RyR1, as previous studies were performed with only 2 mM ATP (Figure 2). However, the precise orientation of ARM210 in the binding site remains uncertain. The presence and orientation of ATP is apparent as the interior of the domain is stable and both are aided by mutagenesis, which provides sound reasoning for the benzothiazepine head group of ARM210 binding to W882; however, the tail is left with no clear density in the periphery of the domain.
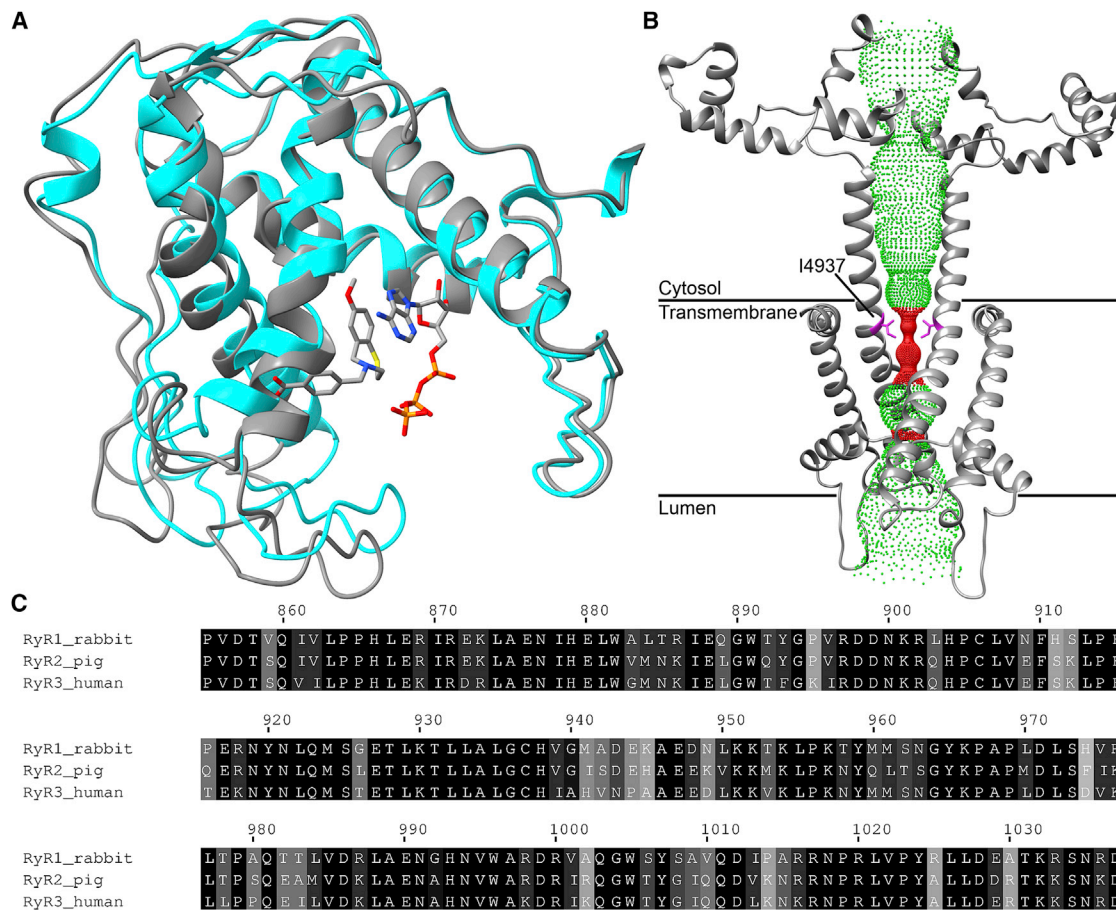
Figure 4. Conformation and conservation

(A) RY1&2 domain in the presence (cyan) and absence (gray) of ARM210. This conformation change results in a global shift that radiates outward to other domains. See also Video S4 for the change in the RY1&2 domain.

(B) The pore of the channel, which was found to be in the closed conformation. The transmembrane pore (residues 4,820–5,037) are depicted as a ribbon diagram of 2 protomers, with the hydrophobic gate residue, I4937, in magenta. The dotted representation of the accessible inner surface of the channel is colored green where the radius exceeds 4 Å and red when the radius is less than 4 Å.

(C) Sequence alignments of the RY1&2 domain (residues 855–1,037). Critical residues are conserved between the 3 isoforms of the RyR, including W882, W996, and C906.

Attempts to deconvolute the binding site with low-pass filtering or 3D classes proved unsuccessful. 3D classes were performed with 3, 4, and 10 classes, as well as iterative rounds of 3D classes, all in Relion. Ultimately, all of the classes were nearly identical and, at best, a small subset of particles could have been discarded. Instead, the mutation of W882 and C906 to alanine confirmed the binding of ARM210 as the stabilizing effects of ARM210 were abolished in this mutant without disrupting the binding of ATP (Figures 2 and 3). This finding is a critically important step toward optimizing the structure of Rycal compounds for efficacy and selectivity, which we aim to accomplish through ongoing collaborative efforts. The positioning of ARM210 with respect to W882 and W996 and the interactions made with ATP will allow for customization of future Rycal compounds to take advantage of these interactions and potentially eliminate ambiguity in the binding site. Optimization of Rycals may take advantage of the high density of the positively charged residues in the RY1&2 domain, including H879, R886, R897, K901, R902, H904, and R918 on the periphery and H993, R998, R1000, R1016, R1017, and R1020 on the interior.

We hypothesize that this binding site is also a metabolic sensor as it only binds one ATP compared to two ADP, with ADP showing distinct competition with Rycal binding (Figure 2; Table 2), although further structural analyses will be necessary to adequately assess this.

While the elucidation of the mechanism of Rycal compounds likely requires the solving of a calstabin-depleted disease-state structure, the discovery of this binding site adds further context and consideration for structural and physiological studies of RyR channel gating where previous studies were limited to the C-terminal ATP-binding site, which binds simultaneously with the N-terminal site at physiological levels of ATP (Chirasani et al., 2021; des Georges et al., 2016; Lindsay et al., 2018; Ogawa et al., 2021; Porta et al., 2012; Zalk and Marks, 2017). While these results represent a significant advance in studying the effective treatment of the RyR in a host of highly prevalent diseases, the lack of changes in the calstabin-binding site continues to add to the critical importance of resolving the structure of the RyR in disease states. Nonetheless, the discovery of the
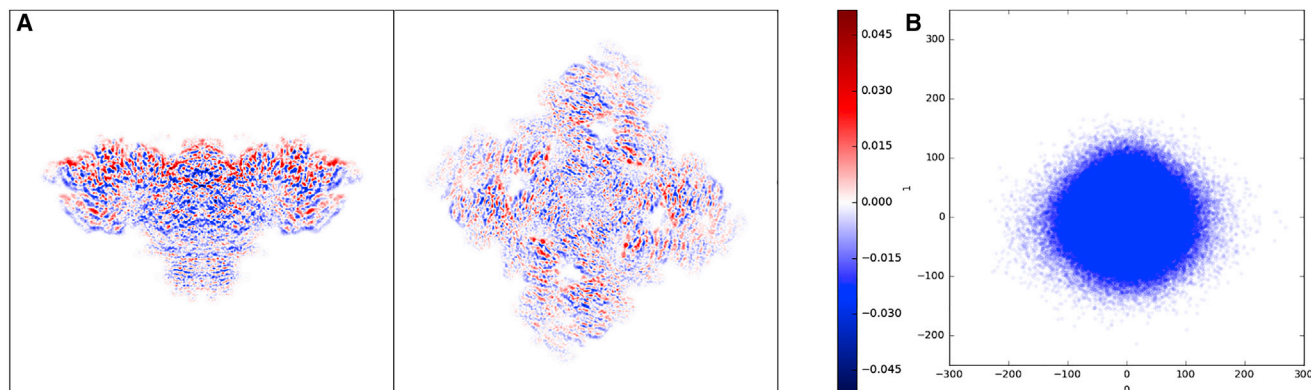
Figure 5. 3D variability
(A) Side and top-down slices showing no variation in the pore of the channel in the presence of ARM210 despite activating ligands (Ca^{2+}, ATP, and caffeine), as indicated by the lack of coloration through the center of the channel.
(B) Reaction coordinate scatterplot of the eigenvectors of the individual particles resolved by 3D variability. The extent of variability is shown along arbitrary axes and indicates that only 1 state is observed in the presence of ARM210.

Rycal and ATP binding site should allow for the creation of new, more specific Rycal compounds and serves as the foundation for future work in studying the interactions of the RyR1 with endogenous ligands such as ATP and ADP, related therapeutic compounds, and in the elucidation of the mechanism of the Rycal compounds in reassociating calstabin-1 with the RyR1 in disease states.

STAR★METHODS

Detailed methods are provided in the online version of this paper and include the following:

- KEY RESOURCES TABLE
- RESOURCE AVAILABILITY
  - Lead contact
  - Materials availability
  - Data and code availability
- EXPERIMENTAL MODEL AND SUBJECT DETAILS
  - Animals
- METHOD DETAILS
  - Mutagenesis, expression, and H$_2$O$_2$ treatment of recombinant RyR1
  - Ligand binding
  - Purification of recombinant calmodulin and TEV protease
  - Purification of native RyR1
  - Grid preparation
  - Cryo-EM data collection & processing
  - SR vesicle preparation and Rycal treatment
  - Planar lipid bilayers
  - Ca^{2+} imaging in HEK293 cells expressing WT and mutant RyR1 channels
- QUANTIFICATION AND STATISTICAL ANALYSIS

SUPPLEMENTAL INFORMATION

Supplemental information can be found online at https://doi.org/10.1016/j.str.2022.04.010.

AUTHOR CONTRIBUTIONS

Conceptualization, Z.M., S.R., O.B.C., and A.R.M.; methodology, Z.M., H.D., Q.Y., and S.R.; investigation, Z.M., H.D., Q.Y., S.R., A.W., and Y.L.; visualization, Z.M., H.D., Q.Y., and S.R.; funding acquisition, A.R.M.; project administration, A.R.M.; supervision, O.B.C. and A.R.M.; writing – original draft, Z.M., Q.Y., and S.R.; writing – review & editing, Z.M., O.B.C., and A.R.M.

REFERENCES

Acimovic, I., Refaat, M.M., Moreau, A., Salykin, A., Reiken, S., Sleiman, Y., Souidi, M., Pribyl, J., Kajava, A.V., Richard, S., et al. (2018). Post-translational modifications and diastolic calcium leak associated to the novel RyR2-D3638A mutation lead to CPVT in patient-specific hiPSC-derived cardiomyocytes. J. Clin. Med. 7, 423. https://doi.org/10.3390/jcm7110423.

Adams, P.D., Afonine, P.V., Bunkóczi, G., Chen, V.B., Davis, I.W., Echols, N., Headd, J.J., Hung, L.-W., Kapral, G.J., Grosse-Kunstleve, R.W., et al. (2010). PHENIX: a comprehensive Python-based system for macromolecular structure solution. Acta Crystallogr. D Biol. Crystallogr. 66, 213–221. https://doi.org/10.1107/s0907444909052925.

Andersson, D.C., Betzenhauser, M.J., Reiken, S., Meli, A.C., Umanskaya, A., Xie, W., Shiomi, T., Zalk, R., Lacampagne, A., and Marks, A.R. (2011). Ryanodine receptor oxidation causes intracellular calcium leak and muscle weakness in aging. Cell Metab. *14*, 196–207. https://doi.org/10.1016/j.cmet.2011.05.014.

Andersson, D.C., and Marks, A.R. (2010). Fixing ryanodine receptor Ca(2+) leak - a novel therapeutic strategy for contractile failure in heart and skeletal muscle. Drug Discov. Today Dis. Mech. *7*, e151–e157. https://doi.org/10.1016/j.ddmec.2010.09.009.

Bellinger, A.M., Reiken, S., Carlson, C., Mongillo, M., Liu, X., Rothman, L., Matecki, S., Lacampagne, A., and Marks, A.R. (2009). Hypernitrosylated ryanodine receptor calcium release channels are leaky in dystrophic muscle. Nat. Med. *15*, 325–330. https://doi.org/10.1038/nm.1916.

Bellinger, A.M., Reiken, S., Dura, M., Murphy, P.W., Deng, S.X., Landry, D.W., Nieman, D., Lehnart, S.E., Samaru, M., LaCampagne, A., and Marks, A.R. (2008). Remodeling of ryanodine receptor complex causes "leaky" channels: a molecular mechanism for decreased exercise capacity. Proc. Natl. Acad. Sci. U S A. *105*, 2198–2202. https://doi.org/10.1073/pnas.0711074105.

Brillantes, A.M.B., Ondrias, K., Scott, A., Kobrinsky, E., Ondriasová, E., Moschella, M.C., Jayaraman, T., Landers, M., Ehrlich, B.E., and Marks, A.R. (1994). Stabilization of calcium release channel (ryanodine receptor) function by FK506-binding protein. Cell *77*, 513–523. https://doi.org/10.1016/0092-8674(94)90214-3.

Cabra, V., Murayama, T., and Samsó, M. (2016). Ultrastructural analysis of self-associated RyR2s. Biophysical J. *110*, 2651–2662. https://doi.org/10.1016/j.bpj.2016.05.013.

Capogrosso, R.F., Mantuano, P., Uaesoontrachoon, K., Cozzoli, A., Giustino, A., Dow, T., Srinivassane, S., Filipovic, M., Bell, C., Vandermeulen, J., et al. (2018). Ryanodine channel complex stabilizer compound S48168/ARM210 as a disease modifier in dystrophin-deficient mdx mice: proof-of-concept study and independent validation of efficacy. FASEB J. *32*, 1025–1043. https://doi.org/10.1096/fj.201700182rrr.

Chirasani, V.R., Pasek, D.A., and Meissner, G. (2021). Structural and functional interactions between the Ca(2+)-ATP-and caffeine-binding sites of skeletal muscle ryanodine receptor (RyR1). J. Biol. Chem. *297*, 101040. https://doi.org/10.1016/j.jbc.2021.101040.

des Georges, A., Clarke, O.B., Zalk, R., Yuan, Q., Condon, K.J., Grassucci, R.A., Hendrickson, W.A., Marks, A.R., and Frank, J. (2016). Structural basis for gating and activation of RyR1. Cell *167*, 145–157.e17. https://doi.org/10.1016/j.cell.2016.08.075.

Dridi, H., Liu, X., Yuan, Q., Reiken, S., Yehia, M., Sittenfeld, L., Apostolou, P., Buron, J., Sicard, P., Matecki, S., et al. (2020). Role of defective calcium regulation in cardiorespiratory dysfunction in Huntington's disease. JCI Insight *5*, e140614. https://doi.org/10.1172/jci.insight.140614.

Emsley, P., and Cowtan, K. (2004). Coot: model-building tools for molecular graphics. Acta Crystallogr. Section D *60*, 2126–2132. https://doi.org/10.1107/s0907444904019158.

Fabiato, A., and Fabiato, F. (1978). Calcium-induced release of calcium from the sarcoplasmic reticulum of skinned cells from adult human, dog, cat, rabbit, rat, and frog hearts and from fetal and new-born rat ventricles. Ann. N. Y Acad. Sci. *307*, 491–522. https://doi.org/10.1111/j.1749-6632.1978.tb41979.x.

Fauconnier, J., Thireau, J., Reiken, S., Cassan, C., Richard, S., Matecki, S., Marks, A.R., and Lacampagne, A. (2010). Leaky RyR2 trigger ventricular arrhythmias in Duchenne muscular dystrophy. Proc. Natl. Acad. Sci. U S A. *107*, 1559–1564. https://doi.org/10.1073/pnas.0908540107.

Goddard, T.D., Huang, C.C., Meng, E.C., Pettersen, E.F., Couch, G.S., Morris, J.H., and Ferrin, T.E. (2018). UCSF ChimeraX: meeting modern challenges in visualization and analysis. Protein Sci. *27*, 14–25. https://doi.org/10.1002/pro.3235.

Inui, M., Saito, A., and Fleischer, S. (1987). Purification of the ryanodine receptor and identity with feet structures of junctional terminal cisternae of sarcoplasmic reticulum from fast skeletal muscle. J. Biol. Chem. *262*, 1740–1747. https://doi.org/10.1016/s0021-9258(19)75701-9.

Dubochet, J., Adrian, M., Chang, J.J., Homo, J.C., Lepault, J., McDowall, A.W., and Schultz, P. (1988). Cryo-electron microscopy of vitrified specimens. Q. Rev. Biophys. *21*, 129–228. https://doi.org/10.1017/s0033583500004297.

Kermode, H., Williams, A.J., and Sitsapesan, R. (1998). The interactions of ATP, ADP, and inorganic phosphate with the sheep cardiac ryanodine receptor. Biophys. J. *74*, 1296–1304. https://doi.org/10.1016/s0006-3495(98)77843-9.

Kushnir, A., Santulli, G., Reiken, S.R., Coromilas, E., Godfrey, S.J., Brunjes, D.L., Colombo, P.C., Yuzefpolskaya, M., Sokol, S.I., Kitsis, R.N., and Marks, A.R. (2018). Ryanodine receptor calcium leak in circulating B-lymphocytes as a biomarker in heart failure. Circulation *138*, 1144–1154. https://doi.org/10.1161/circulationaha.117.032703.

Kushnir, A., Todd, J.J., Witherspoon, J.W., Yuan, Q., Reiken, S., Lin, H., Munce, R.H., Wajsberg, B., Melville, Z., Clarke, O.B., et al. (2020). Intracellular calcium leak as a therapeutic target for RYR1-related myopathies. Acta Neuropathol. *139*, 1089–1104. https://doi.org/10.1007/s00401-020-02150-w.

Lacampagne, A., Liu, X., Reiken, S., Bussiere, R., Meli, A.C., Lauritzen, I., Teich, A.F., Zalk, R., Saint, N., Arancio, O., et al. (2017). Post-translational remodeling of ryanodine receptor induces calcium leak leading to Alzheimer's disease-likepathologies and cognitive deficits. Acta Neuropathologica *134*, 749–767. https://doi.org/10.1007/s00401-017-1733-7.

Lehnart, S.E., Mongillo, M., Bellinger, A., Lindegger, N., Chen, B.-X., Hsueh, W., Reiken, S., Wronska, A., Drew, L.J., Ward, C.W., et al. (2008). Leaky Ca(2+) release channel/ryanodine receptor 2 causes seizures and sudden cardiac death in mice. J. Clin. Invest. *118*, 2230–2245. https://doi.org/10.1172/jci35346.

Lehnart, S.E., Terrenoire, C., Reiken, S., Wehrens, X.H.T., Song, L.-S., Tillman, E.J., Mancarella, S., Coromilas, J., Lederer, W.J., Kass, R.S., and Marks, A.R. (2006). Stabilization of cardiac ryanodine receptor prevents intracellular calcium leak and arrhythmias. Proc. Natl. Acad. Sci. U S A *103*, 7906–7910. https://doi.org/10.1073/pnas.0602133103.

Lehnart, S.E., Wehrens, X.H.T., Laitinen, P.J., Reiken, S.R., Deng, S.-X., Cheng, Z., Landry, D.W., Kontula, K., Swan, H., and Marks, A.R. (2004). Sudden death in familial polymorphic ventricular tachycardia associated with calcium release channel (ryanodine receptor) leak. Circulation *109*, 3208–3214. https://doi.org/10.1161/01.cir.0000132472.98675.ec.

Liebschner, D., Afonine, P.V., Baker, M.L., Bunkóczi, G., Chen, V.B., Croll, T.I., Hintze, B., Hung, L.W., Jain, S., McCoy, A.J., et al. (2019). Macromolecular structure determination using X-rays, neutrons and electrons: recent developments in Phenix. Acta Crystallogr D Struct Biol. *75*, 861–877.

Lindsay, C., Sitsapesan, M., Chan, W.M., Venturi, E., Welch, W., Musgaard, M., and Sitsapesan, R. (2018). Promiscuous attraction of ligands within the ATP binding site of RyR2 promotes diverse gating behaviour. Sci. Rep. *8*, 15011. https://doi.org/10.1038/s41598-018-33328-8.

Liu, X., Betzenhauser, M.J., Reiken, S., Meli, A.C., Xie, W., Chen, B.X., Arancio, O., and Marks, A.R. (2012). Role of leaky neuronal ryanodine receptors in stress-induced cognitive dysfunction. Cell *150*, 1055–1067. https://doi.org/10.1016/j.cell.2012.06.052.

Ma, R., Haji-Ghassemi, O., Ma, D., Jiang, H., Lin, L., Yao, L., Samurkas, A., Li, Y., Wang, Y., Cao, P., et al. (2020). Structural basis for diamide modulation of ryanodine receptor. Nat. Chem. Biol. *16*, 1246–1254. https://doi.org/10.1038/s41589-020-0627-5.

Marx, S.,O., Gaburjakova, J., Gaburjakova, M., Henrikson, C., Ondrias, K., and Marks Andrew, R. (2001). Coupled gating between cardiac calcium release channels (ryanodine receptors). Circ. Res. *88*, 1151–1158. https://doi.org/10.1161/hh1101.091268.

Marx, S.O., Ondrias, K., and Marks, A.R. (1998). Coupled gating between individual skeletal muscle Ca2+ release channels (ryanodine receptors). Science *281*, 818–821. https://doi.org/10.1126/science.281.5378.818.

Marx, S.O., Reiken, S., Hisamatsu, Y., Jayaraman, T., Burkhoff, D., Rosemblit, N., and Marks, A.R. (2000). PKA phosphorylation dissociates FKBP12.6 from the calcium release channel (ryanodine receptor). Cell *101*, 365–376. https://doi.org/10.1016/s0092-8674(00)80847-8.

Matecki, S., Dridi, H., Jung, B., Saint, N., Reiken, S.R., Scheuermann, V., Mrozek, S., Santulli, G., Umanskaya, A., Petrof, B.J., et al. (2016). Leaky ryanodine receptors contribute to diaphragmatic weakness during mechanical ventilation. Proc. Natl. Acad. Sci. U S A. *113*, 9069–9074. https://doi.org/10.1073/pnas.1609707113.

Mei, Y., Xu, L., Kramer, H.F., Tomberlin, G.H., Townsend, C., and Meissner, G. (2013). Stabilization of the skeletal muscle ryanodine receptor ion channel-FKBP12 complex by the 1,4-benzothiazepine derivative S107. PLoS One *8*, e54208. https://doi.org/10.1371/journal.pone.0054208.

Melville, Z., Kim, K., Clarke, O.B., and Marks, A.R. (2021). High-resolution structure of the membrane-embedded skeletal muscle ryanodine receptor. Structure *30*, 172–180.e3. https://doi.org/10.2210/pdb7m6l/pdb.

Nakai, J., Dirksen, R.T., Nguyen, H.T., Pessah, I.N., Beam, K.G., and Allen, P.D. (1996). Enhanced dihydropyridine receptor channel activity in the presence of ryanodine receptor. Nature *380*, 72–75. https://doi.org/10.1038/380072a0.

Ogawa, H., Kurebayashi, N., Yamazawa, T., and Murayama, T. (2021). Regulatory mechanisms of ryanodine receptor/Ca(2+) release channel revealed by recent advancements in structural studies. J. Muscle Res. Cell Motil. *42*, 291–304. https://doi.org/10.1007/s10974-020-09575-6.

Pettersen, E.F., Goddard, T.D., Huang, C.C., Meng, E.C., Couch, G.S., Croll, T.I., Morris, J.H., and Ferrin, T.E. (2021). UCSF ChimeraX: Structure visualization for researchers, educators, and developers. Protein Sci. *30*, 70–82. https://doi.org/10.1002/pro.3943.

Pettersen, E.F., Goddard, T.D., Huang, C.C., Couch, G.S., Greenblatt, D.M., Meng, E.C., and Ferrin, T.E. (2004). UCSF Chimera—a visualization system for exploratory research and analysis. J. Comput. Chem. *25*, 1605–1612. https://doi.org/10.1002/jcc.20084.

Porta, M., Diaz-Sylvester, P.L., Neumann, J.T., Escobar, A.L., Fleischer, S., and Copello, J.A. (2012). Coupled gating of skeletal muscle ryanodine receptors is modulated by Ca2+, Mg2+, and ATP. Am. J. Physiol. Cell Physiol. *303*, C682–C697. https://doi.org/10.1152/ajpcell.00150.2012.

Punjani, A., Rubinstein, J.L., Fleet, D.J., and Brubaker, M.A. (2017). cryoSPARC: algorithms for rapid unsupervised cryo-EM structure determination. Nat. Methods *14*, 290–296. https://doi.org/10.1038/nmeth.4169.

Reiken, S., Wehrens Xander, H.T., Vest John, A., Barbone, A., Klotz, S., Mancini, D., Burkhoff, D., and Marks Andrew, R. (2003). β-Blockers restore calcium release channel function and improve cardiac muscle performance in human heart failure. Circulation *107*, 2459–2466. https://doi.org/10.1161/01.cir.0000068316.53218.49.

Rohou, A., and Grigorieff, N. (2015). CTFFIND4: fast and accurate defocus estimation from electron micrographs. J. Struct. Biol. *192*, 216–221. https://doi.org/10.1016/j.jsb.2015.08.008.

Rubinstein, J.L., and Brubaker, M.A. (2015). Alignment of cryo-EM movies of individual particles by optimization of image translations. J. Struct. Biol. *192*, 188–195. https://doi.org/10.1016/j.jsb.2015.08.007.

Samsó, M. (2017). A guide to the 3D structure of the ryanodine receptor type 1 by cryoEM. Protein Sci. *26*, 52–68. https://doi.org/10.1002/pro.3052.

Santulli, G., Pagano, G., Sardu, C., Xie, W., Reiken, S., D'Ascia, S.L., Cannone, M., Marziliano, N., Trimarco, B., Guise, T.A., et al. (2015). Calcium release channel RyR2 regulates insulin release and glucose homeostasis. J. Clin. Invest. *125*, 1968–1978. https://doi.org/10.1172/jci79273.

Schneider, C.A., Rasband, W.S., and Eliceiri, K.W. (2012). NIH Image to ImageJ: 25 years of image analysis. Nat. Methods *9*, 671–675. https://doi.org/10.1038/nmeth.2089.

Shan, J., Betzenhauser, M.J., Kushnir, A., Reiken, S., Meli, A.C., Wronska, A., Dura, M., Chen, B.-X., and Marks, A.R. (2010). Role of chronic ryanodine receptor phosphorylation in heart failure and β-adrenergic receptor blockade in mice. J. Clin. Invest. *120*, 4375–4387. https://doi.org/10.1172/jci37649.

Shan, J., Xie, W., Betzenhauser, M., Reiken, S., Chen, B.-X., Wronska, A., and Marks, A.R. (2012). Calcium leak through ryanodine receptors leads to atrial fibrillation in 3 mouse models of catecholaminergic polymorphic ventricular tachycardia. Circ. Res. *111*, 708–717. https://doi.org/10.1161/circresaha.112.273342.

Smart, O.S., Goodfellow, J.M., and Wallace, B.A. (1993). The pore dimensions of gramicidin A. Biophys J. *65*, 2455–2460. https://doi.org/10.1016/S0006-3495(93)81293-1.

Smart, O.S., Neduvelil, J.G., Wang, X., Wallace, B.A., and Sansom, M.S.P. (1996). HOLE: a program for the analysis of the pore dimensions of ion channel structural models. J. Mol. Graphics *14*, 354–360. https://doi.org/10.1016/s0263-7855(97)00009-x.

Stagg, S.M., Noble, A.J., Spilman, M., and Chapman, M.S. (2014). ResLog plots as an empirical metric of the quality of cryo-EM reconstructions. J. Struct. Biol. *185*, 418–426. https://doi.org/10.1016/j.jsb.2013.12.010.

Suloway, C., Pulokas, J., Fellmann, D., Cheng, A., Guerra, F., Quispe, J., Stagg, S., Potter, C.S., and Carragher, B. (2005). Automated molecular microscopy: the new Leginon system. J. Struct. Biol. *151*, 41–60. https://doi.org/10.1016/j.jsb.2005.03.010.

Tan, Y.Z., Baldwin, P.R., Davis, J.H., Williamson, J.R., Potter, C.S., Carragher, B., and Lyumkis, D. (2017). Addressing preferred specimen orientation in single-particle cryo-EM through tilting. Nat. Methods *14*, 793–796. https://doi.org/10.1038/nmeth.4347.

Tung, C.C., Lobo, P.A., Kimlicka, L., and Van Petegem, F. (2010). The amino-terminal disease hotspot of ryanodine receptors forms a cytoplasmic vestibule. Nature *468*, 585–588. https://doi.org/10.1038/nature09471.

Wagenknecht, T., Grassucci, R., and Frank, J. (1988). Electron microscopy and computer image averaging of ice-embedded large ribosomal subunits from Escherichia coli. J. Mol. Biol. *199*, 137–147. https://doi.org/10.1016/0022-2836(88)90384-1.

Waning, D.L., Mohammad, K.S., Reiken, S., Xie, W., Andersson, D.C., John, S., Chiechi, A., Wright, L.E., Umanskaya, A., Niewolna, M., et al. (2015). Excess TGF-β mediates muscle weakness associated with bone metastases in mice. Nat. Med. *21*, 1262–1271. https://doi.org/10.1038/nm.3961.

Wehrens, X.H.T., Lehnart, S.E., Huang, F., Vest, J.A., Reiken, S.R., Mohler, P.J., Sun, J., Guatimosim, S., Song, L.-S., Rosemblit, N., et al. (2003). FKBP12.6 deficiency and defective calcium release channel (ryanodine receptor) function linked to exercise-induced sudden cardiac death. Cell *113*, 829–840. https://doi.org/10.1016/s0092-8674(03)00434-3.

Wehrens, X.H.T., Lehnart, S.E., Reiken, S., van der Nagel, R., Morales, R., Sun, J., Cheng, Z., Deng, S.-X., de Windt, L.J., Landry, D.W., and Marks, A.R. (2005). Enhancing calstabin binding to ryanodine receptors improves cardiac and skeletal muscle function in heart failure. Proc. Natl. Acad. Sci. U S A *102*, 9607–9612. https://doi.org/10.1073/pnas.0500353102.

Wehrens, X.H.T., Lehnart, S.E., Reiken, S., Vest, J.A., Wronska, A., and Marks, A.R. (2006). Ryanodine receptor/calcium release channel PKA phosphorylation: a critical mediator of heart failure progression. Proc. Natl. Acad. Sci. U S A. *103*, 511–518. https://doi.org/10.1073/pnas.0510113103.

Wehrens, X.H.T., Lehnart, S.E., Reiken, S.R., Deng, S.-X., Vest, J.A., Cervantes, D., Coromilas, J., Landry, D.W., and Marks, A.R. (2004). Protection from cardiac Arrhythmia through ryanodine receptor-stabilizing protein Calstabin2. Science *304*, 292–296. https://doi.org/10.1126/science.1094301.

Woll, K.A., Haji-Ghassemi, O., and Van Petegem, F. (2021). Pathological conformations of disease mutant Ryanodine Receptors revealed by cryo-EM. Nat. Commun. *12*, 807. https://doi.org/10.1038/s41467-021-21141-3.

Yano, M., Ono, K., Ohkusa, T., Suetsugu, M., Kohno, M., Hisaoka, T., Kobayashi, S., Hisamatsu, Y., Yamamoto, T., Kohno, M., et al. (2000). Altered stoichiometry of FKBP12.6 versus ryanodine receptor as a cause of Abnormal Ca2+ leak through ryanodine receptor in heart failure. Circulation *102*, 2131–2136. https://doi.org/10.1161/01.cir.102.17.2131.

Zalk, R., Clarke, O.B., des Georges, A., Grassucci, R.A., Reiken, S., Mancia, F., Hendrickson, W.A., Frank, J., and Marks, A.R. (2015). Structure of a mammalian ryanodine receptor. Nature *517*, 44–49. https://doi.org/10.1038/nature13950.

Zalk, R., and Marks, A.R. (2017). Ca(2+) release channels join the 'resolution revolution. Trends Biochem. Sci. *42*, 543–555. https://doi.org/10.1016/j.tibs.2017.04.005.

STAR★METHODS

KEY RESOURCES TABLE

REAGENT or RESOURCE	SOURCE	IDENTIFIER
Biological Samples		
New Zealand white rabbit	BioIVT	Cat #RAB00MSCUZN
Chemicals, Peptides, and Recombinant Proteins		
Phosphatidylcholine	Avanti	Cat# 441601G
1,2-dioleoyl-sn-glycero-3-phosphocholine	Avanti	Cat# 850375C
Lipofectamine 2000	ThermoFisher	Cat # 11668027
X-tremeGENE 9 DNA Transfection Reagent	Millipore Sigma	Cat# 6365787001
PKA catalytic subunit	Millipore Sigma	Cat # P2645
Critical Commercial Assays		
HiTrap Q HP column	Cytiva	Cat# 17115401
QuikChange II XL Site-Directed Mutagenesis Kit	Agilent	Cat# 200521
Deposited Data		
RyR1-ATP-ARM210 model	This paper	PDB ID: 7TZC
RyR1-ATP-ARM210 map	This paper	EMDB ID: 26205
RyR1-ATP-ARM210 raw data	This paper	EMPIAR ID: 10997
WT Pig RyR1, apoCAM, class 1 & 2, closed	Woll et a., 2021	PDB ID: 6X32
Rabbit RyR1 (Caffeine/ATP/Ca2+, class 3&4)	des Georges et al. (2016)	PDB ID: 5TAQ
Oligonucleotides		
rRyR1-W882A forward GAACATCCATGAACTC(**GC**G)GCGCTGACGCGCATT	This paper	N/A
rRyR1-W996A forward GAATGGGCATAACGTG(GCG)GCACGAGACCGAGTG	This paper	N/A
rRyR1-C906A forward CAAGAGGCTGCACCCG(**GCA**)CT**A**GTGAACTTCCACAGCC	This paper	N/A
Software and Algorithms		
cryoSPARC	Punjani et al. (2017)	https://cryosparc.com/
Leginon	Suloway et al. (2005)	https://sbgrid.org/software/titles/leginon
Phenix	Liebschner et al., 2019	https://www.phenix-online.org/
Coot	Emsley and Cowtan (2004)	https://www.ccpem.ac.uk/
HOLE	Smart et al., 1993	http://www.holeprogram.org/
Chimera	Pettersen et al. (2004)	https://www.cgl.ucsf.edu/chimera/
ChimeraX	Pettersen et al., 2021	https://www.cgl.ucsf.edu/chimerax/
Clampfit 10.2	Molecular Devices	https://www.moleculardevices.com/
ImageJ	Schneider et al. (2012)	https://imagej.nih.gov/ij/download.html
Other		
UltrAuFoil Holey gold grids	Quantifoil	R 0.6/1.0, Au 300

RESOURCE AVAILABILITY

Lead contact
Further information and requests for resources and reagents should be directed to and will be fulfilled by the lead contact, Andrew R. Marks (arm42@cumc.columbia.edu).

Materials availability
This study did not generate new unique reagents.

Data and code availability

cryoEM data have been deposited at PDB (7TZC), EMDB (EMD-26205), and EMPIAR (EMPIAR-10997) and are publicly available as of the date of publication. Accession numbers are listed in the Key resources table. All data reported in this paper will be shared by the Lead contact upon request.

This paper does not report original code.

Any additional information required to reanalyze the data reported in this paper is available from the Lead contact upon request.

EXPERIMENTAL MODEL AND SUBJECT DETAILS

Animals

Rabbit tissue used for the purification of RyR1 was New Zealand white rabbit, age and gender unspecified, purchased from BioIVT.

METHOD DETAILS

Mutagenesis, expression, and H_2O_2 treatment of recombinant RyR1

Constructs expressing wild-type, W882A, W996A, and C906A RyR1 were formed by introducing the respective mutations into fragments of rabbit RyR1 using QuikChange II XL Site-Directed Mutagenesis Kit (Agilent) with an HpaI-HpaI fragment in a pBlueScript vector. Each fragment was subcloned into a full length RyR1 construct in pcDNA3.1 vector using an HpaI restriction enzyme. Mutagenesis was confirmed by sequencing and expressed in 293T/17 cells using Lipofectamine 2000 (Thermo Fisher Scientific). The primers used to introduce specific mutations (codons in parentheses, mutated nucleotides in bold) are as follows: rRyR1-W882A-F GAACATCCATGAACTC(**GC**G)GCGCTGACGCGCATT, rRyR1-W996A-F GAATGGGCATAACGTG(GCG)GCACGAGACCGAGTG, and rRyR1-C906A-F CAAGAGGCTGCACCCG(**GCA**)CT**A**GTGAACTTCCACAGCC. For each mutant, the second primer was the complementary reverse to the forward primer. HEK293 cells grown in DMEM supplemented with 10% (v/v) FBS (Invitrogen), 100 U/mL penicillin, 100 μg/mL streptomycin, and 2 mM L-glutamine were co-transfected with WT or mutant RyR1 cDNA using X-tremeGENE 9 DNA Transfection Reagent (Roche). Cells were collected 48 h after transfection.

ER vesicles from HEK293 cells expressing RyR1-WT or RyR1-mutant were prepared by homogenizing cell pellets on ice using a Teflon glass douncer (50 times) with two volumes of: 20 mM Tris-maleate pH 7.4, 1 mM EDTA, 1 mM DTT, and protease inhibitors (Roche). Homogenate was then centrifuged at 4,000xg for 15 min at 4°C. The resulting supernatant was centrifuged at 40,000xg for 30 min at 4°C. The final pellet, containing the ER fractions, was resuspended and aliquoted in 250 mM sucrose, 10 mM MOPS pH 7.4, 1 mM EDTA, 1 mM DTT and protease inhibitors. Samples were frozen in liquid nitrogen and stored at −80°C. For PKA-phosphorylated channel experiments, ∼200 μg of microsomes were in vitro phosphorylated with 40 units of PKA catalytic subunit (SigmaAldrich) for 30 min at 30°C in the presence of the following buffer: 50 mM Tris/PIPES pH 7.0, 8 mM $MgCl_2$, 1 mM MgATP, and 1 mM EGTA. The samples were then centrifuged for 10 min at 100kxg. The resulting pellets were washed four times with wash buffer (300 mM sucrose, 10 mM imidazole, pH 7.4) and aliquots were frozen in liquid nitrogen and stored at −80°C. Oxidation of RyR1 was induced by incubating microsomes with 1 mM H_2O_2 for 30 min at room temperature prior to washing.

Ligand binding

^3H-S107 binding was used in place of ARM210 due to the unavailability of tritiated ARM210. S107 and ARM210 were supplied by ARMGO Pharma. Inc. which was compensated for the cost of goods. S107 is a first generation Rycal compound lacking the benzoic acid moiety of ARM210. Titrative ^3H-S107 binding, performed in the absence and presence of 10 mM NaATP, was initiated by addition of ^3H-S107 (10–10,000 nM final concentration) to 0.1 mg skeletal sarcoplasmic reticulum (SR) microsomes in binding buffer (50 mM Tris-HCl, pH 7.5, 150 mM NaCl, 25 mM $MgCl_2$). For ATP and ADP competition, S107 binding was assessed at a concentration of 1 μM. All samples were incubated at room temperature for 30 min ^3H-S107 binding was stopped by addition of ice-cold binding buffer prior to filtration through GF/B Whatman filters pre-equilibrated with 0.015% PE. Filters were washed 3 times with 5 mL of wash buffer (10 mM MOPS, 200 mM NaCl, pH 7.4), dried, and counted. Data were normalized to ^3H-ryanodine binding. Nonspecific binding was determined using 20-fold excess unlabeled S107.

^{32}P-ATP and ^{32}P-ADP binding were initiated by addition of the respective radioligands (100–50,000 nM) to 0.1 mg recombinant RyR1 microsomes in binding buffer. Samples were incubated at room temperature for 60 min and the reaction was stopped as previously described. Data were normalized to ^3H-ryanodine binding and ligand binding affinities and stoichiometries for each assay are summarized in Table 2.

Purification of recombinant calmodulin and TEV protease

All purification steps were performed on ice unless otherwise stated. Recombinant homo sapien calmodulin (CaM) was expressed in BL21 (DE3) E. coli cells with a N-terminal 6-histidine tag and a tobacco etch virus (TEV) protease cleavage site. Protein expression was induced with 0.8 mM IPTG added to E. coli at an OD_{600} of 0.8 with overnight incubation at 18°C prior to centrifugation for 10 min at 6500xg and storage at −80°C. CaM was purified using a two-step HisTrap (5 mL, GE Healthcare Life Sciences) column purification. In brief, the pellets were resuspended in buffer A (20 mM HEPES pH 7.5, 150 mM NaCl, 20 mM Imidazole, 5 mM BME, 0.5 mM AEBSF) and lysed using an emulsiflex (Avestin EmulsiFlex-C3). The lysate was pelleted by centrifugation for 10 min at 100kxg. The supernatant

was then loaded over a HisTrap FF column and washed with 5 CV of buffer A to remove contaminants prior to elution using a linear gradient from buffer A to buffer B (buffer A containing 500 mM Imidazole). Fractions containing CaM were pooled, 1–2 mg of purified TEV protease was added, and the mixture was dialyzed overnight at 4°C into buffer C (buffer A with no imidazole). CaM was then loaded onto a HisTrap HP column with the flowthrough collected and the wash fractionated to retain fractions containing CaM prior to elution of TEV and any remaining contaminants with a linear gradient from buffer C to buffer B. The flowthrough and any fractions containing CaM were pooled, concentrated to >2 mM, determined by spectroscopy using a NanoDrop 1000 (ThermoFisher) with abs @ 280 nm and the extinction coefficient of CaM. CaM was stored at −20°C. TEV protease was purified in the same manner with the exception of using an uncleavable his-tag and thus ending after the first HisTrap column wherein the purified protease was stored at −80°C in buffer C with 10% glycerol.

Purification of native RyR1

All purification steps were performed on ice unless otherwise stated. RyR1 was purified from rabbit skeletal muscle with modifications to the previously published methodology. Rabbit back and thigh muscle tissue was harvested and snap frozen in liquid nitrogen immediately following euthanasia prior to shipping on dry ice and storage at −80°C (BioIVT). Following this, 20 g of frozen rabbit muscle was resuspended and lysed in 200 mL buffer A (10 mM tris maleate pH 6.8, 1 mM EGTA, 1 mM benzamidine hydrochloride, 0.5 mM AEBSF) via blending with a Waring blender. The resulting suspension was pelleted by centrifugation for 10 min at 11,000xg. The supernatant was filtered through cheesecloth to remove debris and the membranes were then pelleted by centrifugation for 30 min at 36,000xg.

The membranes were solubilized in buffer B (10 mM HEPES pH 7.4, 0.8 M NaCl, 1% CHAPS, 0.1% phosphatidylcholine, 1 mM EGTA, 2 mM DTT, 0.5 mM AEBSF, 1 mM benzamidine hydrochloride, one protease inhibitor tablet (Pierce)) prior to homogenization using a glass tissue grinder (Kontes). Homogenization was repeated following the addition of buffer C (buffer B with no NaCl) at a 1:1 ratio with buffer B. The resulting homogenate was centrifugation for 30 min at 100kxg. The supernatant was then vacuum filtered and incubated with excess, purified CaM for 30 min prior to loading onto a HiTrap Q HP column (5 mL, GE Healthcare Life Sciences) at 1 mL/min. This column was pre-equilibrated with buffer D (10 mM HEPES pH 7.4, 400 mM NaCl, 1.0% CHAPS, 1 mM EGTA, 0.5 mM TCEP, 0.5 mM AEBSF, 1 mM benzamidine hydrochloride, 0.01% 1,2-dioleoyl-sn-glycero-3-phosphocholine (DOPC, Avanti)).

DOPC, dissolved in chloroform, was evaporated under nitrogen gas and resuspended in buffer D. Contaminating proteins were washed away with six column volumes (CV) of buffer D prior to elution of RyR1 with a linear gradient from 480 to 550 mM NaCl using buffers D and E (buffer D with 600 mM NaCl). RyR1-containing fractions were pooled and concentrated to 10 mg/mL using 100,000 kDa cut-off centrifugation filters (MilliporeSigma) prior to addition of 10 mM NaATP, 0.5 mM ARM210, 5 mM caffeine, and 30 μM Ca^{2+}_{free}. Free Ca^{2+} concentrations were calculated using MaxChelator. Final RyR1 concentration was 8.4 mg/mL (15 μM), determined by spectroscopy using a NanoDrop 1000 Spectrophotometer (ThermoFisher, 1 abs @ 280 nm = 1 mg/mL).

Grid preparation

UltrAuFoil holey gold grids (Quantifoil R 0.6/1.0, Au 300) were plasma cleaned with H_2 and O_2 (Gatan). 3 μL of the purified native RyR1 sample was applied to each grid. Grids were then blotted for 6.5 s at blot force 3, with a wait time of 30 s and no drain time, prior to vitrification by plunge freezing into liquid ethane chilled with liquid nitrogen with a Vitrobot Mark IV (ThermoFisher) operated at 4°C with 100% relative humidity (Dubochet et al., 1988; Wagenknecht et al., 1988). Ashless filter paper (Whatman) was used to limit Ca^{2+} contamination.

Cryo-EM data collection & processing

Prepared grids were screened in-house on a Glacios Cryo-TEM (ThermoFisher) microscope with a 200-kV x-FEG source and a Falcon 3EC direct electron detector (ThermoFisher). Microscope operations and data collection were carried out using EPU software (ThermoFisher). High resolution data collection was performed at Columbia University on a Titan Krios 300-kV (ThermoFisher) microscope equipped with an energy filter (slit width 20 eV) and a K3 direct electron detector (Gatan). Data were collected using Leginon (Suloway et al., 2005) and at a nominal magnification of 105,000× in electron counting mode, corresponding to a pixel size of 0.826 Å. The electron dose rate was set to 16 e⁻/pixel/sec with 2.5 s exposures for a total dose of 57.65 e/Å².

CryoEM data processing was performed in cryoSPARC (Punjani et al., 2017; Rohou and Grigorieff, 2015; Rubinstein and Brubaker, 2015; Stagg et al., 2014; Tan et al., 2017) with image stacks aligned using Patch motion, defocus value estimation by Patch CTF estimation. Particle picking was performed using the template picker with pre-existing templates. 333,010 particles were initially picked from 6,862 micrographs and these were subjected to 2D classification in cryoSPARC with 50 classes. 154,000 particles from the highest-resolution classes were pooled for ab initio 3D reconstruction with a single class followed by homogenous refinement with C4 symmetry imposed. Symmetry expansion was performed prior to local refinement with three separate masks. The first mask was composed of the N-terminal domains, the SPRY domains, the RY1&2 domain, calstabin, and calmodulin. The second mask surrounded the bridging-solenoid, and the third mask surrounded the pore of the RyR. Only the pore mask utilized C4 symmetry. The resulting maps were combined in Chimera (Pettersen et al., 2004) to generate a composite map prior to calibration of the pixel size using correlation coefficients with a map generated from the crystal structure of the N-terminal domain (2XOA) (Tung et al., 2010). The pixel size was altered by 0.001 Å per step, up to 10 steps in each direction with an initial and final pixel size of 0.826 and 0.833 Å, respectively. Model building was performed in Coot (Emsley and Cowtan, 2004) starting with an unpublished model. Real-space refinement was performed in Phenix (Adams et al., 2010; Liebschner et al., 2019). Figures of the final structure were created using

Chimera (Pettersen et al., 2004) and ChimeraX (Goddard et al., 2018). Quantification of the pore radius was calculated using HOLE (Smart et al., 1996) and chemical structures were drawn in ChemDraw. CryoEM statistics are summarized in Table 1 and Figure S2.

SR vesicle preparation and Rycal treatment

HEK293 cell pellets were homogenized in 1 mM tris-maleate buffer (pH 7.4) in the presence of protease inhibitors (Roche), and centrifuged at 8,000 rpm (5,900xg) for 20 min at 4°C. The supernatant was ultracentrifuged at 32,000 rpm (100,000xg) for 45 min at 4°C. The final pellet containing microsomal fractions enriched in SR vesicles was resuspended and aliquoted in 300 mM sucrose, 5 mM Pipes (pH 7.0) containing protease inhibitors (Roche) (Kushnir et al., 2020). Samples were frozen in liquid nitrogen and stored at −80°C. 10 μM S107 or ARM210 was added to microsomes overnight at 4°C.

Planar lipid bilayers

Planar lipid bilayers were formed using a 3:1 mixture of phosphatidylethanolamine and phosphatidylcholine (Avanti Polar Lipids) suspended (30 mg/mL) in decane by painting the lipid/decane solution across a 200 μm aperture in a polysulfonate cup (Warner Instruments) separating two chambers. The *trans* chamber (1 mL) representing the intra-SR (luminal) compartment was connected to the headstage input of a bilayer voltage clamp amplifier (BC-525D, Warner Instruments) and the *cis* chamber (1 mL), representing the cytoplasmic compartment, was held at virtual ground. Solutions in both chambers were as follows: 1 mM EGTA, 250/125 mM Hepes/Tris, 50 mM KCl, 0.64 mM $CaCl_2$, pH 7.35 as *cis* solution and 250 mM Hepes, 53 mM $Ca(OH)_2$, 50 mM KCl, pH 7.35 as *trans* solution (Kushnir et al., 2020; Matecki et al., 2016).

The concentration of free Ca^{2+} in the *cis* chamber was calculated using the WinMaxC program (version 2.50; www.stanford.edu/~cpatton/maxc.html). SR vesicles were added to the *cis* side, and fusion with the lipid bilayer was induced by making the *cis* side hyperosmotic by addition of 400–500 mM KCl. After the appearance of potassium and chloride channels, the cis compartment was perfused with the *cis* solution. Single-channel currents were recorded at 0 mV using a Bilayer Clamp BC-535 amplifier (Warner Instruments), filtered at 1 kHz, and digitized at 4 kHz. All experiments were performed at room temperature. Data acquisition was performed using Digidata 1440A and Axoscope 10.2 software, recordings were analyzed using Clampfit 10.2 (Molecular Devices). Open probability was identified by 50% threshold analyses using a minimum of 2 min of continuous record. At the conclusion of each experiment, 5 μM ryanodine was added to the *cis* chamber to confirm channels as RyR.

Ca^{2+} imaging in HEK293 cells expressing WT and mutant RyR1 channels

Cytosolic Ca^{2+} measurements were performed with HEK293 cells expressing WT or mutant RyR1 grown on a glass-bottom dish for 26–30 h after plasmid transfection. To induce RyR1 oxidation, the transfected cells were incubated with 1 mM H_2O_2 for 30 min at 37°C, then washed 3 times with PBS. Treated cells were incubated with ARM210 (10 μM) overnight. HEK293 cells were loaded with 4 μM fluo-4 AM in culture medium for 30 min at 37°C and then incubated with Krebs solution (140 mM NaCl, 5 mM KCl, 2 mM $CaCl_2$, 1 mM $MgCl_2$, 11 mM glucose, and 5 mM HEPES, pH 7.4). Imaging experiments were performed at room temperature (26°C). Caffeine was prepared in Krebs solution and added to the cells at 10 mM. Confocal imaging was performed by excitation with a 488 nm light from the argon laser of a Zeiss LSM 800 inverted confocal microscope (40× oil immersion lens). Data were analyzed using ImageJ software (Schneider et al., 2012). Experiments were replicated 3 times. n ≥ 30 cells per group. Data are means ± SEM, One-way-ANOVA shows *p < 0.05; **p < 0.01, versus WT.

QUANTIFICATION AND STATISTICAL ANALYSIS

Cryo-EM data were processed using cryoSPARC. Quantification of the pore radius was calculated using HOLE (Figure 4). Cryo-EM structural statistics were analyzed using Phenix (Table 1). Reported map resolutions are based on the 0.143 Fourier Shell Correlation criterion (Figure S2 and Table 1). The reported map resolutions and 3days variability were calculated using cryoSPARC (Figures 5 and S2).

Radioligand binding data were normalized to ^{3}H-ryanodine binding (Figure 2). Nonspecific binding was determined using 20-fold excess unlabeled S107. These data were processed using Excel and each experiment was performed four times. The error bars represent the standard deviation.

Single channel recording data were acquired using Digidata 1440A and Axoscope 10.2 software and analyzed using Clampfit 10.2 (Molecular Devices) (Figure 3). Open probability was identified by 50% threshold analyses using a minimum of 2 min of continuous recording. Calcium imaging data were analyzed using ImageJ software (Schneider et al., 2012) (Figure 3). Single channel and calcium imaging experiments were repeated at least 3 times. n ≥ 30 cells per group. Data are means ± SEM, One-way-ANOVA shows *p < 0.05; **p < 0.01, versus. WT.